

Constraining gravitational wave velocities using gravitational and electromagnetic wave observations of white dwarf binaries

Tian-Yong Cao,^{1,2} Ankit Kumar,^{1*} and Shu-Xu Yi^{1†}

¹Key Laboratory of Particle Astrophysics, Institute of High Energy Physics, Chinese Academy of Sciences, 19B Yuquan Road, Beijing 100049, People's Republic of China

²University of Chinese Academy of Sciences, Chinese Academy of Sciences, Beijing 100049, People's Republic of China

Accepted 2024 July 16. Received 2024 June 24; in original form 2024 April 8

ABSTRACT

Although the general theory of relativity (GR) predicts that gravitational waves (GWs) have exactly the same propagation velocity as electromagnetic (EM) waves, many theories of gravity beyond GR expect otherwise. Accurate measurement of the difference in their propagation speed, or a tight constraint on it, could be crucial to validate or put limits on theories beyond GR. The proposed future space-borne GW detectors are poised to detect a substantial number of Galactic white dwarf binaries (GWDBs), which emit the GW as semi-monochromatic signals. Concurrently, these GWDBs can also be identified as optical variable sources. Here we proposed that allocating a GWDB's optical light curve and contemporaneous GW signal can be used to trace the difference between the velocity of GW and EM waves. Simulating GW and EM wave data from 14 verification binaries (VBs), our method constrains propagation-originated phase differences, limiting the discrepancy between the speed of light (c) and GW (c_{GW}). Through the utilization of LISA's design sensitivity and the current precision in optical observation on GWDB, our study reveals that a four-year observation of the 14 recognized VBs results in a joint constraint that confines $\Delta c/c$ ($\Delta c = c_{\text{GW}} - c$) to the range of -2.1×10^{-12} and 4.8×10^{-12} . Additionally, by incorporating this constraint on c_{GW} , we are able to establish boundaries for the mass of the graviton, limiting it to $m_g \leq 3 \times 10^{-23} \text{ eV}/c^2$, and for the parameter associated with local Lorentz violation, \bar{s}_{00} , constrained within the range of $-3.4 \times 10^{-11} \leq \bar{s}_{00} \leq 1.5 \times 10^{-11}$.

Key words: Gravitational waves – White dwarf

1 INTRODUCTION

Following Einstein's proposal of the general theory of relativity (GR) in 1915, he theoretically forecasted the existence of gravitational waves (GW) (Einstein 1916, 1918). According to his prediction, the speed of GW was expected to be precisely equal to the speed of light (Maggiore 2007). Further exploration into the realm of gravity has prompted certain researchers to propose alternative theories, a few of which involve modifications to the speed of GW. For example, if the graviton possesses a non-vanishing mass, its velocity would be dispersed in a vacuum as (Fan et al. 2017):

$$\frac{c_{\text{GW}}}{c} = \left(1 - \frac{m_g^2 c^4}{E^2}\right)^{1/2} \approx 1 - \frac{1}{2} \frac{m_g^2 c^4}{E^2}, \quad (1)$$

where m_g is the mass of graviton; c and c_{GW} are the speed of light and GW respectively; and $E = hf$ is the energy of the graviton, where h is the Planck constant and f is the frequency of GW. The predicted dispersion pattern of gravitational waves (GW) has served as a means to investigate the mass of gravitons, causing phase differences among diverse frequency components of GW, and thereby

causing alterations in its waveform, formally a 1 post-Newtonian order term (Will 1998; Scientific et al. 2016):

$$\Phi(f) = -\frac{\pi D c}{\lambda_{\text{GW}}^2 (1+z) f}, \quad (2)$$

where $\lambda_{\text{GW}} = h/(m_g c)$ is the graviton's Compton wavelength, z is the cosmological redshift and D is the cosmological distance as defined explicitly in Will (1998). By aligning the observed waveform with its theoretical projection (Cutler et al. 1993), we can establish confidence intervals for the graviton's wavelength or mass. Employing a similar methodology, the LIGO and Virgo collaboration utilized gravitational wave events GW150914, GW170104, and GW170817 to establish upper limits for the mass of gravity, which were set at $1.2 \times 10^{-22} \text{ eV}/c^2$, $7.7 \times 10^{-23} \text{ eV}/c^2$, $9.51 \times 10^{-22} \text{ eV}/c^2$ (Scientific et al. 2016, 2018; Abbott et al. 2019), respectively. Correspondingly, at 1 kHz, the upper limits on $\Delta c/c$ from the above mentioned GW events stands at $< 4.2 \times 10^{-22}$, 1.7×10^{-22} , and 2.64×10^{-22} , where $\Delta c = c_{\text{GW}} - c$. This constraint is notably stringent, nevertheless presuming $c_{\text{GW},\infty} = c$, wherein $c_{\text{GW},\infty}$ represents the velocity of gravitational waves at an infinitely high frequency. Subsequent discussion will unveil that additional methods, independent of this particular assumption, are still required. Moreover, if alternative methods can impose constraints on c_{GW} in a much lower frequency regime, it could, in turn, restrict the possible range of the graviton's mass.

* E-mail: kumarankit@ihep.ac.cn

† E-mail: sxyi@ihep.ac.cn

Table 1. A Summary outlining the constraints obtained by utilizing various methods. Refs.: [1] (Scientific et al. 2016), [2] (Scientific et al. 2018), [3] (Abbott et al. 2019), [4] (Abbott et al. 2017b), [5] (Cornish et al. 2017), [6] (Liu et al. 2020), [7] (Larson & Hiscock 2000), [8] (Cutler et al. 2003).

| Method | Result | Refs. |
|-------------------------------|--|-------|
| GW dispersion | $\frac{\Delta c}{c} < 1.7 \times 10^{-22}$ | 1,2,3 |
| time-lag: GRB & GW | $-3 \times 10^{-15} \leq \frac{\Delta c}{c} \leq +7 \times 10^{-16}$ | 4 |
| time-lag: two GW detectors | $-0.03 \leq \frac{\Delta c}{c} \leq +0.02$ | 5,6 |
| GWDBs ¹ | $\frac{\Delta c}{c} < 3 \times 10^{-12}$ | 7,8 |

A theoretical framework known as the Standard Model extension (SME) characterizes general violations of Lorentz and CPT invariance in both general relativity and the standard model at attainable energies (Kostelecký & Mewes 2016; Mewes 2019). In the context of SME, the GW velocity will be corrected to:

$$\frac{c_{\text{GW},\pm}}{c} = 1 - \zeta^0 \pm |\zeta|. \quad (3)$$

where $c_{\text{GW},\pm}$ represents the velocity of the two polarizations of GW. If $|\zeta|$ is non-zero, birefringence will occur. With ζ^0 exerting notable dominance over the $|\zeta|$ term, as highlighted by Kostelecký & Mewes (2016), one can safely opt to exclude consideration of $|\zeta|$ in their calculations (Liu et al. 2020). Consequently, our attention is solely on the deviation value ζ^0 in this context. This approximation allows us to expand the GW velocity employing the spherical harmonic function:

$$\begin{aligned} \frac{c_{\text{GW}}}{c}(\alpha, \delta) &= 1 + \frac{1}{2} \sum_{jm} (-1)^j Y_{jm}(\alpha, \delta) \bar{s}_{jm} \\ &= 1 + \sum_j (-1)^j \left(\frac{1}{2} \bar{s}_{j0} Y^{j0} \right. \\ &\quad \left. + \sum_{m>0} [\Re \bar{s}_{jm} \Re Y_{jm} - \Im \bar{s}_{jm} \Im Y_{jm}] \right), \end{aligned} \quad (4)$$

where $\Re x$ and $\Im x$ represent the real and imaginary parts of x . Y_{jm} is a spherical harmonic function, therefore m should be an integer satisfying $-j \leq m \leq j$. Within the SME framework, it is posited that $j \leq 2$. In order to constrain the nine coefficients present in the above equation, a minimum of nine GW sources, each with their respective c_{GW} limits and corresponding sky positions, are needed.

There are several other ways to put constraints on the c_{GW} . One of the stringent constraints arises from the time difference between GW170817 and GRB170817A (Goyal et al. 2021; Li et al. 2016). On 2017 August 17, the GW event GW170817 was observed by LIGO, and the associated gamma-ray burst (GRB) GRB170817A was observed independently by the Fermi Gamma-ray Burst Monitor (GBM). There is a 1.74 ± 0.05 s delay between the prompt emission of GRB170817A and the chirp time of GW170817 (Abbott et al. 2017b). The observed time lag between the GW170817's peak and

the first photon of GRB 170817A was used to constrain on the fractional speed difference to $-3 \times 10^{-15} \leq \Delta c/c \leq +7 \times 10^{-16}$ (Abbott et al. 2017a). The result depends on the assumption of the intrinsic emission time difference between the GW and GRB, which is a debating presumption. (Ciolfi & Siegel 2015; Rezzolla & Kumar 2015; Tsang et al. 2012) A previous simulation study (Hendriks et al. 2023) showed that the joint detection of GW and its GRB prompt-emission counterpart will be a rare event. Therefore, we would expect obtaining a sample of c_{GW} from at least nine different sources with this method, to be challenging in a short time scale.

There are also other model/source-independent methods, such as using the time difference between two detectors at large distances to the same GW signal. For example, the LIGO at the Hanford and Livingston sites have a time difference of about 10 milliseconds. Cornish et al. (2017) used a Bayesian approach, combining data from the first three LIGO GW observations, to constrain c_{GW} to $-0.45 \leq \Delta c/c \leq +0.42$. Subsequently, Liu et al. (2020) further narrowed the interval to $-0.03 \leq \Delta c/c \leq +0.02$ with more data and constrained the coefficient \bar{s}_{00} within $-0.2 < \bar{s}_{00} < 0.07$.

Another model-independent method yielding more stringent constraints involves utilizing GW and EM signals emitted by Galactic white dwarf binaries (GWDB) (Larson & Hiscock 2000). It's believed there are roughly 11.5 billion white dwarfs (WD) in our Galaxy (Napiwotzki 2009), and a significant proportion of these will come together to form binary systems that steadily emit GW. In general, the frequency of these emitted GWs are below 10^{-3} Hz (Barke et al. 2014; Amaro-Seoane et al. 2023) and cannot be detected effectively by ground-based GW detectors like LIGO, Virgo, and KAGRA. However, within a certain range, there are tens of millions of GWDBs that could be detected by space-borne GW detectors like LISA (Kupfer et al. 2018), TianQin (Huang et al. 2020; Ren et al. 2023) or Taiji (Ruan et al. 2020). There are several known GWDBs, whose binary parameters are well measured with optical observation, and they can be effectively detected by space-borne GW detectors. Those GWDBs are usually referred to as verification GWDBs or verification binaries (VBs).

In 2000, Larson & Hiscock (2000) suggested comparing the potential phase difference between the GW and optical signals of GWDB to constrain the graviton's mass. In their work, they used the ratio between the sampling time and the total integration time to estimate the error in phase measurements. In addition, they focused on the errors caused by refraction due to interstellar medium refraction in the EM wave propagation processes and the initial phase difference at the source between the GW and EM signals. Later, Cutler et al. (2003) specifically discussed the phase error in GW measurements on GWDB, correcting the error to:

$$\Delta\phi_{\text{GW}} = \frac{\alpha}{2} \left(\frac{S}{N} \right)^{-1} [1 + O(S/N)^{-1}], \quad (5)$$

where α is a correction term from the initial phase difference from the GW and EM signals. Moreover, they estimated the constrain to the graviton's Compton wavelength as $\lambda_g > 35 \times 10^{12}$ km. They used analytical error propagation estimation and did not include the intrinsic phase discrepancy between GW and EM counterpart signals. All methods for measuring $\Delta c/c$ and the corresponding results (including the limits from real observation and the estimated level of limits from proposed methods) are summarized in Table 1.

Here in the present work, we use simulation to consider the phase error of EM and GW altogether with more sources and also include the intrinsic phase difference between EM and GW due to polarization angle. We simulate the signals of GW and EM emitted by the VBs, and then fit the phase difference between the received signals.

¹ It is an estimation of the proposed method, instead of constraints from real observation.

Table 2. The observed parameters of VBs: The contents in each column of the table are, in order, the name of the source, right ascension, declination, orbital period, GWDB masses, distance, orbital inclination, 4-year SNR in LISA, and references. Refs.: [1] (Burdge et al. 2019a), [2] (Kupfer et al. 2018), [3] (Brown et al. 2011), [4] (Hermes et al. 2012), [5] (Kilic et al. 2014), [6] (Brown et al. 2020), [7] (Burdge et al. 2019b), [8] (Brown et al. 2010), [9] (Geier et al. 2013), [10] (Kilic et al. 2011).

| Source | α /deg | δ /deg | P /s | m_1 / M_\odot | m_2 / M_\odot | d /kpc | i /deg | SNR (4 years) | Refs. |
|------------|------------------|------------------|---------|----------------------|----------------------|-----------|-------------|------------------|-------|
| J1539+5027 | 234.88 | 50.46 | 414.79 | 0.61 | 0.21 | 2.34 | 84.15 | 143 | 1 |
| J0651+2844 | 102.89 | 28.74 | 765.5 | 0.26 | 0.5 | 0.933 | 86.9 | 90.1 | 2,3,4 |
| J0935+4411 | 143.78 | 44.19 | 1188 | 0.312 | 0.75 | 0.645 | 60 | 44.9 | 2,5 |
| J0923-1218 | 140.96 | -12.31 | 252.36 | 0.344 | 0.19 | 0.262 | 60 | 31 | 6 |
| J1638+3500 | 249.61 | 35.00 | 1186.12 | 0.698 | 0.45 | 0.103 | 60 | 30 | 6 |
| J0130+5321 | 22.74 | 53.36 | 518.53 | 0.191 | 0.4 | 0.085 | 60 | 24 | 6 |
| J1738+2927 | 264.65 | 29.46 | 242.43 | 0.261 | 0.55 | 0.78 | 60 | 24 | 6 |
| J1115+0246 | 168.86 | 2.77 | 1071.79 | 0.446 | 0.26 | 0.899 | 60 | 16 | 6 |
| J0533+0209 | 83.38 | 2.15 | 1233.97 | 0.652 | 0.167 | 1.5 | 72.8 | 15.2 | 7 |
| J1401-0817 | 210.33 | -8.29 | 278.92 | 0.216 | 0.79 | 0.555 | 60 | 13 | 6 |
| J1048-0000 | 162.11 | -0.0158 | 521.12 | 0.169 | 0.62 | 0.707 | 60 | 6.3 | 6 |
| J0923+3028 | 140.94 | 30.47 | 3383.68 | 0.275 | 0.76 | 0.299 | 60 | 5.6 | 2,8 |
| CD-3011223 | 212.82 | -30.88 | 4231.8 | 0.54 | 0.79 | 0.337 | 82.9 | 4.9 | 2,9 |
| J1630+4233 | 247.63 | 42.555 | 2389.8 | 0.298 | 0.76 | 1.019 | 60 | 4.6 | 2,10 |

we exclude the initial phase differences and obtain an estimation of the phase differences due to propagation, and thus constraints on $\Delta c/c$. The VBs utilized in this paper, along with their binary parameters, are presented in Table 2.

The adopted method will be described in detail in the next section. In Section 3, we will focus on the intrinsic phase difference between GW and EM. In Section 4, we will discuss the method of simulating GW data. The process of optical light curve signal simulation will be outlined in Section 5. Section 6 will demonstrate how we match the phases using a joint fit and unveil our findings. Sections 7 and 8 are dedicated to exploring the boundaries of physical quantities and discussing the improvements.

2 METHODOLOGY OVERVIEW

The time variation of the strain of the two polarization modes of GW for a non-evolving circular GWDB can be approximated by the quadrupole moment, which is derived by Maggiore (2007) to vary sinusoidally. The response in the detector is a linear combination of the two modes in a certain proportion. (Huang et al. 2020) This proportion, known as the antenna pattern, will be provided with its specific expression in the next section. Therefore, the response in the GW detector can be represented with:

$$h(t) \propto \sin(2\pi f_{\text{GW}}t + \phi_{0,\text{GW}}), \quad (6)$$

while the variance in the EM properties can be represented with:

$$A(t) \propto \sin(2\pi f_{\text{EM}}t + \phi_{0,\text{EM}}), \quad (7)$$

with $f_{\text{GW}} = n f_{\text{EM}}$. For the WDs utilized in this paper, the EM properties that can be readily measured and exhibit a simple sinusoidal

period include apparent magnitude ² (a.m.) and radial velocity ³ (r.v.). (Burdge et al. 2019a; Kupfer et al. 2018; Brown et al. 2011; Hermes et al. 2012; Kilic et al. 2014; Brown et al. 2020; Burdge et al. 2019b; Brown et al. 2010; Geier et al. 2013; Kilic et al. 2011) It is worth noting that both the GW and a.m. data vary at twice the orbital frequency, while the r.v. varies at an equal frequency. Thus in the above equation, $n = 1$ stands for a.m. and $n = 2$ for r.v.. For the present scenario, we are considering the GW and EM signals received at the solar barycentre, assuming that the time and phase shift due to the relative motion between the detectors and the solar barycentre have been perfectly corrected ⁴. The phase difference is:

$$\phi_{0,\text{GW}} - n\phi_{0,\text{EM}} = \Delta\phi_{\text{int}} + \Delta\phi_{\text{prop}}, \quad (8)$$

with $\Delta\phi_{\text{int}}$ representing the intrinsic phase difference between EM wave and GW. In the present work, we set the phase of the EM wave as fiducial, and the main intrinsic phase offset is due to the polarization

² The a.m. is defined by $m_x = -2.5 \log_{10} \left(\frac{F_x}{F_{x,0}} \right)$, where F_x is the observed flux using spectral filter x and $F_{x,0}$ is the reference flux (zero-point) for that photometric filter

³ The r.v. is velocity projection in the radial direction. It is derived from the Doppler red/blue-shift in high quality spectroscopic observations, which need more observation resources and thus there are less available data points in Fig.3.

⁴ The relative motion between the detectors (optical telescopes and LISA) and the solar barycentre will introduce annual sinusoidal structures into the signals (due to geometrical delay and Doppler effect). If such noises are not corrected, any phase difference between GW and optical light curve can be dominated by such noise, and can not be used for our purpose. Luckily, such effects can be corrected as a standard procedure as the ephemeris of the Earth, the geolocation of the telescopes, and the orbital parameters of the LISA spacecrafts are known with high accuracies (Cutler 1998). We, therefore, assume we can directly work with data with such effects corrected.

Table 3. The table of polarization phases and the main parameters with their uncertainties: The data in each column of the table are, in order, the value and uncertainty of right ascension, declination, orbital inclination, and the polarization phases. The uncertainties of RA and DEC are from GAIA (Provencal et al. 1997; Vallanari et al. 2023), and the RA, DEC, orbital inclination and the uncertainties of inclination is from (Kupfer et al. 2018). The uncertainty of right ascension and declination is presented in the unit "mas" which refers to milliarcseconds.

| Source | α /deg | $\Delta\alpha$ /mas | δ /deg | $\Delta\delta$ /mas | i /deg | Δi /deg | φ_0 /rad | $\Delta\varphi_0$ /rad |
|------------|------------------|------------------------|------------------|------------------------|-------------|--------------------|---------------------|---------------------------|
| J1539+5027 | 234.88 | 0.4911 | 50.46 | 0.4823 | 84.15 | 0.64 | -1.1313 | 0.0422 |
| J0651+2844 | 102.89 | 0.3093 | 28.74 | 0.2825 | 86.9 | 1 | -1.4257 | 0.0446 |
| J0935+4411 | 143.78 | 0.4814 | 44.19 | 0.4117 | 60 | 2 | -0.8686 | 0.0178 |
| J0923-1218 | 140.96 | 0.0446 | -12.31 | 0.0400 | 60 | 2 | -0.4168 | 0.0141 |
| J1638+3500 | 249.61 | 0.0213 | 35.00 | 0.0281 | 60 | 2 | -0.2981 | 0.0111 |
| J0130+5321 | 22.74 | 0.0210 | 53.36 | 0.0219 | 60 | 2 | -0.1993 | 0.0087 |
| J1738+2927 | 264.65 | 0.1801 | 29.46 | 0.2340 | 60 | 2 | -0.6239 | 0.0174 |
| J1115+0246 | 168.86 | 0.2711 | 2.77 | 0.2880 | 60 | 2 | -0.5295 | 0.0158 |
| J0533+0209 | 83.38 | 0.2169 | 2.15 | 0.1978 | 72.8 | 1.4 | -0.8166 | 0.0334 |
| J1401-0817 | 210.33 | 0.0679 | -8.29 | 0.0502 | 60 | 2 | 1.3545 | 0.0082 |
| J1048-0000 | 162.11 | 0.1692 | -0.016 | 0.1278 | 60 | 2 | -0.3598 | 0.0128 |
| J0923+3028 | 140.94 | 0.0471 | 30.47 | 0.0370 | 60 | 2 | 1.5140 | 0.0038 |
| CD-3011223 | 212.82 | 0.0442 | -30.88 | 0.0457 | 82.9 | 0.4 | -1.2674 | 0.0157 |
| J1630+4233 | 247.63 | 0.1615 | 42.55 | 0.1768 | 60 | 2 | -0.3158 | 0.0115 |

of the GW, which will be discussed in detail in the subsequent section. $\Delta\phi_{\text{prop}}$ denotes the phase difference induced during the propagation, which reflects the potential difference between c and c_{GW} :

$$\Delta\phi_{\text{prop}} = 2D \frac{2\pi}{P} (1/c_{\text{GW}} - 1/c) \approx -\frac{4\pi D}{P} \frac{\Delta c}{c^2}, \quad (9)$$

where P is the orbital period of the GWDB. Consequently, we can obtain the desired quantity i.e. Δc as:

$$\Delta c = \frac{c^2 P}{4\pi D} (n\phi_{\text{EM}} - \phi_{0,\text{GW}} + \Delta\phi_{\text{int}}), \quad (10)$$

The following sections will illustrate our approach to restricting the phases separately, allowing us to then establish a restriction on Δc .

3 INTRINSIC PHASE DIFFERENCE

The intrinsic phase difference $\Delta\phi_{\text{int}}$ comprises several components, with the polarization phase being the most significant one. The GW strain recorded by the detector can be described as a linear combination of the two GW polarizations modulated by the detector's response:

$$h(t) = \frac{\sqrt{3}}{2} A_+ F^+ \cos 2\pi f t + \frac{\sqrt{3}}{2} A_\times F^\times \sin 2\pi f t \quad (11)$$

$$= \mathcal{A} \sin(2\pi f t + \varphi_0),$$

where $\mathcal{A} = \frac{\sqrt{3}}{2} \sqrt{(A_+ F^+)^2 + (A_\times F^\times)^2}$ is the combined amplitude, $\varphi_0 = \arctan(-\frac{A_+ F^+}{A_\times F^\times})$ is the polarization phase and $A_{+,\times}$ are the amplitudes of the two GW polarization, which can be represented as:

$$A_+(i) = \mathcal{A}_0 (1 + \cos^2 i); \quad (12)$$

$$A_\times(i) = 2\mathcal{A}_0 \cos i,$$

where i refers to the orbital inclination and $\mathcal{A}_0 = \frac{2(GM)^{3/5}}{c^4 d} (\pi f_{\text{GW}})^{2/3}$ (Huang et al. 2020). Here M is the chip mass and d is the distance. The $F^{+,\times}$ are defined as the antenna pattern functions and can be mathematically represented as:

$$F^+(\theta_s, \phi_s, \psi_s) = \frac{1}{2} (1 + \cos^2 \theta_s) \cos 2\phi_s \cos 2\psi_s$$

$$- \cos \theta_s \sin 2\phi_s \sin 2\psi_s; \quad (13)$$

$$F^\times(\theta_s, \phi_s, \psi_s) = \frac{1}{2} (1 + \cos^2 \theta_s) \cos 2\phi_s \sin 2\psi_s$$

$$+ \cos \theta_s \sin 2\phi_s \cos 2\psi_s,$$

where ψ_s is the polarization angle; (θ_s, ϕ_s) are the latitude and longitude of the source in the detector's coordinate frame, which can be transformed from Right Ascension (RA) and Declination (DEC) as in Huang et al. (2020). Further, we also estimated the uncertainties of the polarization phase φ_0 due to uncertainties in sky position, inclination, and polarization angle.

We apply the Monte Carlo algorithm to calculate the phase uncertainty. We input randomly generated RA, DEC, inclination, and polarization angle values from 1000 normal distributions into the above equations. This process calculates the phase, allowing us to derive the polarization phase values with distribution. The main parameters with their uncertainties are shown in Table 3, where the uncertainties of RA and DEC are from GAIA (Provencal et al. 1997; Vallanari et al. 2023), and other data is borrowed from Kupfer et al. (2018). Besides, we take polarization angle $\psi_s = 30^\circ$ with the uncertainty $\Delta\psi_s = 10^{-3}$, which is supported from Huang et al. (2020). The

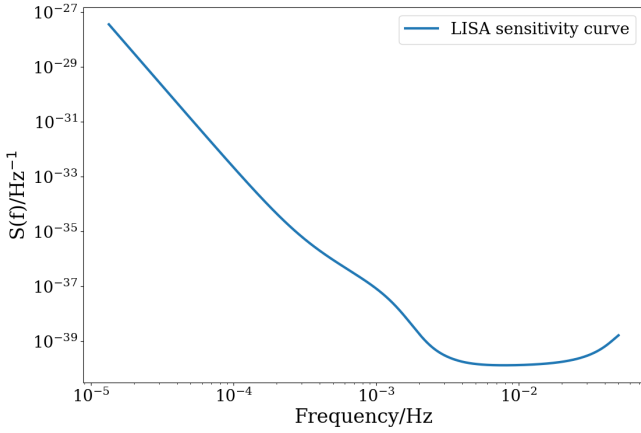


Figure 1. The sensitivity curve of LISA depicted in (Robson et al. 2019).

polarization phase and its associated uncertainties are also presented in Table 3.

Additional intrinsic phase difference will be introduced between the GW and the a.m. signals, when the VB are not in tidal synchronization (Larson & Hiscock 2000; Cutler et al. 2003). In this case, the elongated axes of WDs can be misaligned with the line of masses. According to Burkart et al. (2013); Fuller & Lai (2012); Yu et al. (2020), detached VBs with orbital period less than 20 min can be considered tidally synchronized, where this additional intrinsic phase difference disappears. Therefore, when considering the a.m. light curves, we limit the sample to those detached VBs with period less than 20 min. It results in only one VB in the sample: J0533+0209. We like to note that, although there are theoretical arguments that this system can be in tidal synchronization, there lacks support from observation. We therefore present two version of results, one is with the assumption that J0533+0209 is in tidal synchronization and its a.m. light curve are used, the other one is when we do not make such assumption, and we use its r.v. data instead.

4 GW SIMULATION

In the following section, we will employ simulation techniques to explore the accuracy with which we can determine the phase of gravitational waves. Here, we aim to implement several simplifications:

First, we assume that the eccentricity of VBs has a negligible effect on the GW phase estimation. Typically, the trajectory of a GWDB deviates from a perfectly circular orbit and instead follows an elliptical trajectory characterized by a specific eccentricity. In practical terms, determining the eccentricity involves considerable uncertainty in measurement. However, the VBs utilized in this context are estimated to possess small eccentricity, allowing a circular orbit to serve as a reliable approximation. In the next section, we will observe that the radial velocities of all sources vary sinusoidally, indicating that their orbits are nearly circular. Moreover, the gravitational waves (GW) emitted by elliptical orbits have evolved from their initial simple, single-frequency sine waveforms into a more complex composition, now characterized by a superposition of multiple harmonics, as discussed in (Maggiore 2007), thereby intensifying the intricacy of the model. This paper, however, focuses on a more simplified scenario involving circular orbits. Our aim here is to test the fundamental principles of this novel method. Integrating the effects of eccentricity into the application of this method while fitting the

data with the model remains a straightforward task. Thus, considering the aim of model simplification, we've opted to streamline these gravitational wave database sets to circular orbits.

The second simplification involves assuming that the orbital frequency of VBs remains static without any evolution. In reality, as GWDBs continuously emit GWs, their frequencies naturally escalate. Therefore, it becomes essential to explore how these fluctuations in frequency might impact subsequent research outcomes. Typically, LISA missions operate for a span of 4-5 years. Our main focus lies in evaluating whether the gravitational wave frequencies will exhibit substantial alterations within this 5-year time frame.

We use `evol` in LEGWORK (Wagg et al. 2022) to calculate the SNR. Take source J0533+0209 as an example, its orbital period change in 5 years is 4.76×10^{-4} s, the cyclical rate of change is 3.02×10^{-12} s/s, which is close to the results measured by Burdge et al. (2019b), i.e., 3.94×10^{-12} s/s. The ratio of the period variation to the orbital period is 3.86×10^{-7} , which can be considered as a constant period during the mission time period. In the subsequent processing, we will phase-fold the simulated data.

We employ LEGWORK to simulate the GW signals. For a source, the total length of probes in one mission is in the range of 4-5 years, and we therefore simulate 1.2×10^8 s time-scales. Since the orbital period scale is around 10^3 s, to reduce the amount of data, we take the sampling frequency as 10^{-1} Hz, i.e. 10s to measure one data point, in order to clearly visualize the GW signal.

Then we add simulated GW noise onto the signals. We consider only the noise within a frequency window around the GW signal. The width of the frequency window df is the frequency resolution $1/T$, where T is the duration of the data. Here, we assume that the distribution of the noise is normal. Based on the derivation in the Appendix A, the standard deviation of the noise can be given as:

$$\sigma_n = \sqrt{S(f) \cdot \Delta f}. \quad (14)$$

The sensitivity curve, as presented by Robson et al. (2019) and showcased in Figure 1, delineates the correlation between noise strain and its respective frequencies.

In figure 2, we plotted simulated signal and noise from 5000s to 15000s. The noise is filtered in the frequency range from $f_{\text{GW}} - df$ to $f_{\text{GW}} + df$, where $df = 1/T$ is the frequency resolution of the data. In figure 2, $df \sim 10^{-4}$ Hz, while for the data we used below, $df \sim 10^{-7}$ Hz. The corresponding SNR for this data segment is 15.2 in 4 years.

5 SIMULATION OF OPTICAL SIGNALS

For subsequent calculations, we require the optical data to vary sinusoidally as the GW, which excludes a fraction of the eclipsing binaries (though our method can be generalized easily to eclipsing binaries). A study conducted by Kupfer et al. (2018) in 2018 assembled a collection of 16 VBs. After eliminating specific eclipsing binaries and incorporating newly detected GWDBs based on the criteria previously discussed, the dataset was ultimately refined to consist of 14 VBs, as outlined in Table 2.

We also provided the basic information of the optical data of the VBs as shown in Table 4. To compare optical data quantitatively, we use relative root mean square error (RRMSE) (Loève 2017) to measure the quality of optical data:

$$R = \frac{\Delta A_{\text{EM}}}{A_{\text{EM}} \cdot \sqrt{N_{\text{EM}}}}, \quad (15)$$

Table 4. Optical data table of the VBs: The data in each column of the table are, in order, the data volume, uncertainty, and amplitude of r.v. and a.m., R of r.v. and a.m. Refs.: [1] (Burdge et al. 2019a), [2] (Kupfer et al. 2018), [3] (Brown et al. 2011), [4] (Hermes et al. 2012), [5] (Kilic et al. 2014), [6] (Brown et al. 2020), [7] (Burdge et al. 2019b), [8] (Brown et al. 2010), [9] (Geier et al. 2013), [10] (Kilic et al. 2011).

| Source | N_{rv} | ΔA_{rv} /km · s ⁻¹ | A_{rm} /km · s ⁻¹ | N_{am} | ΔA_{am} /mag | A_{am} /mag | R_{rv} ×10 ⁻² | R_{am} ×10 ⁻² | Refs. |
|------------|----------|--|-----------------------------------|----------|-------------------------|------------------|-------------------------------|-------------------------------|-------|
| J1539+5027 | 12 | 43.10 | 550 | | | | 2.26 | | 1 |
| J0651+2844 | 77 | 31 | 616.9 | | | | 0.573 | | 2,3,4 |
| J0935+4411 | 55 | 28.73 | 198.5 | | | | 1.95 | | 2,5 |
| J0923-1218 | 25 | 33.33 | 117 | | | | 5.69 | | 6 |
| J1638+3500 | 25 | 25 | 89.5 | | | | 5.59 | | 6 |
| J0130+5321 | 23 | 25 | 209.1 | | | | 2.49 | | 6 |
| J1738+2927 | 16 | 20.83 | 372.7 | | | | 1.40 | | 6 |
| J1115+0246 | 10 | 25 | 139.9 | | | | 5.65 | | 6 |
| J0533+0209 | 35 | 100 | 618.7 | 5000 | 0.0275 | 0.134 | 2.73 | 0.290 | 7 |
| J1401-0817 | 24 | 8.33 | 346.2 | | | | 0.491 | | 6 |
| J1048-0000 | 17 | 16.67 | 312.8 | | | | 1.29 | | 6 |
| J0923+3028 | 44 | 22 | 296 | | | | 1.12 | | 2,8 |
| CD-3011223 | 95 | 11.67 | 376.6 | | | | 0.318 | | 2,9 |
| J1630+4233 | 21 | 29.27 | 288.1 | | | | 2.22 | | 2,10 |

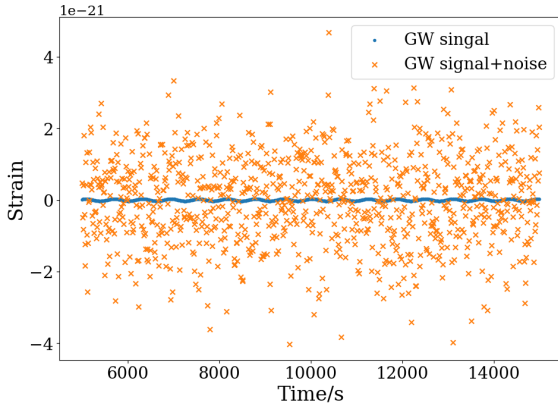


Figure 2. The simulated GW signals within 5000-15000 seconds for J0533-0209 with SNR=15.2 in 4 years.

where R is RRMS, A_{EM} is the optical signal amplitude, ΔA_{EM} is the uncertainty, and N_{EM} is the amount of data. RRMS is the total relative uncertainties of the data, so it can be used to qualify the accuracy of the optical data.

Here, we directly take the optical data as a sinusoidal signal and superimpose on it the error of a normally distributed random function whose standard deviation is the uncertainty of the data. For the temporal distribution, we set the data points uniformly scattered randomly within the GW observation duration.

6 JOINT ANALYSIS AND RESULT

Due to the long time series of the simulation and the large time interval of the optical data, the direct fitting of the signal will produce greater errors. As discussed previously, both the GW data and the optical data have a sinusoidal waveform. Therefore, before formal processing, we first choose to phase fold the signal, i.e., use the obtained time series to invert the corresponding orbital phase value at that moment. The obtained data can demonstrate the measured quantities in one cycle, as shown in Figure 3.

Following this, we applied a curve fitting method to generate phase-shifted data along with the corresponding 90% confidence interval. The fitting function utilized for this purpose is detailed as follows:

$$y = A \sin(n \cdot 2\pi x + \phi), \quad (16)$$

where x , y are the phase and corresponding measurements, respectively, and n is a constant introduced mainly due to the inconsistent periods of GW, r.v., and a.m. In particular, for GW and a.m. $n = 2$ and for r.v. $n = 1$. A and ϕ are the values to be fitted, and the fitted phase ϕ is all we need.

Here, we utilize fitting in order to obtain the expected value of the phase μ with variance σ^2 . Regarding the fitting process, the data distribution is ideally modeled by a T-distribution. However, considering that our dataset sizes are substantial, we approximate the following aspects using a normal distribution, as detailed in (Loève 2017).

For every source, we end up with at least two sets of data, i.e., the GW signal phase distribution $\phi_{GW} \sim N(\mu_{GW}, \sigma_{GW}^2)$ and the optical signal phase distribution $\phi_{EM} \sim N(\mu_{EM}, \sigma_{EM}^2)$. Therefore the distribution of the phase difference between the two should also be normal. Using Eq.10 we can derive the expressions for $\frac{\Delta c}{c}$ as:

Table 5. The limits on $\Delta c/c$ from simulated data: The second column is the relative velocity difference using the optical r.v. data and the next two columns are the upper and lower limits of the 90% confidence interval; columns 5-7 are the same as 2-4, but using a.m. observation instead of r.v. as EM data.

| Source | $\Delta c/c$ (r.v.) | lower limit (r.v.) | Upper limit (r.v.) | $\Delta c/c$ (a.m.) | lower limit (a.m.) | Upper limit (a.m.) |
|------------|-------------------------|-------------------------|------------------------|-------------------------|------------------------|-----------------------|
| J1539+5027 | 1.3×10^{-11} | -0.48×10^{-11} | 3.0×10^{-11} | | | |
| J0651+2844 | 0.27×10^{-11} | -4.7×10^{-11} | 5.3×10^{-11} | | | |
| J0935+4411 | 0.43×10^{-10} | -0.82×10^{-10} | 1.7×10^{-10} | | | |
| J0923-1218 | -0.43×10^{-10} | -3.1×10^{-10} | 2.2×10^{-10} | | | |
| J1638+3500 | 0.27×10^{-9} | -2.3×10^{-09} | 2.9×10^{-09} | | | |
| J0130+5321 | 1.0×10^{-10} | -3.4×10^{-10} | 5.4×10^{-10} | | | |
| J1738+2927 | 0.52×10^{-11} | -1.9×10^{-11} | 2.0×10^{-11} | | | |
| J1115+0246 | -0.21×10^{-10} | -4.0×10^{-10} | 3.6×10^{-10} | | | |
| J0533+0209 | -0.16×10^{-10} | -1.3×10^{-10} | 0.95×10^{-10} | 0.060×10^{-11} | -3.5×10^{-11} | 3.6×10^{-11} |
| J1401-0817 | -0.16×10^{-11} | -1.2×10^{-11} | 0.87×10^{-11} | | | |
| J1048-0000 | -1.4×10^{-11} | -5.2×10^{-11} | 2.3×10^{-11} | | | |
| J0923+3028 | -3.4×10^{-10} | -8.7×10^{-10} | 1.8×10^{-10} | | | |
| CD-3011223 | -1.3×10^{-10} | -4.3×10^{-10} | 1.8×10^{-10} | | | |
| J1630+4233 | 1.4×10^{-10} | -0.34×10^{-10} | 3.2×10^{-10} | | | |

$$\frac{\Delta c}{c} \sim N\left[\frac{Pc}{4\pi D}(\mu_{\text{GW}} - n \cdot \mu_{\text{EM}}), \left(\frac{Pc}{4\pi D}\right)^2(n \cdot \sigma_{\text{EM}}^2 + \sigma_{\text{GW}}^2 + \sigma_{\varphi_0}^2)\right]. \quad (17)$$

The 90% confidence interval of the normal distribution is $(\mu_{\Delta c/c} - 1.645\sigma_{\Delta c/c}, \mu_{\Delta c/c} + 1.645\sigma_{\Delta c/c})$. The upper and lower limits of the confidence intervals have been stated in Table 5.

Based on the assumption that the noises of different VBs in different frequencies are independent (Abbott et al. 2023), the joint probability of $\Delta c/c$ considering all these 14 sources is:

$$p\left(\frac{\Delta c}{c} | d_1, d_2 \dots d_i\right) \propto p\left(\frac{\Delta c}{c} | d_1\right) p\left(\frac{\Delta c}{c} | d_2\right) \dots p\left(\frac{\Delta c}{c} | d_i\right), \quad (18)$$

where i is the number of independent constraints. Since there are 14 sources with both optical r.v. and a.m. data, the value of i should be taken as 14.

For the product of multiple normal distributions, we determine the total expectation and variance using (Loève 2017):

$$\mu = \frac{\sum_i \frac{\mu_i \prod_m \sigma_m^2}{\sigma_i^2}}{\sum_i \frac{\prod_m \sigma_m^2}{\sigma_i^2}}; \quad (19)$$

$$\sigma^2 = \frac{\prod_m \sigma_m^2}{\sum_i \frac{\prod_m \sigma_m^2}{\sigma_i^2}}.$$

Consequently, the final outcome is obtained as $-2.1 \times 10^{-12} \leq \Delta c/c \leq 4.8 \times 10^{-12}$ ($-2.3 \times 10^{-12} \leq \Delta c/c \leq 4.9 \times 10^{-12}$)⁵.

⁵ The results in the parentheses are those if we do not assume tidal synchronization of J0533+0209 and we use its r.v. instead of a.m.. We present the corresponding results in parentheses too in the next section.

7 PHYSICS IMPLICATION

Upon acquiring the constraints on c_{GW} , we can establish limitations on the physical parameters as outlined in Section 1. The mass of the graviton can be obtained from Eq 1 as:

$$m_g = \frac{E}{c^2} \sqrt{-2 \frac{\Delta c}{c}}, \quad c_{\text{gw}} < c. \quad (20)$$

The mass is related to the graviton energy $E = hf$. For GWDBs, the graviton energy is much lower than the GW events detected by LIGO due to their lower frequencies, which enables us to obtain more precise constraints. The distribution of graviton masses is derived by incorporating the constraints from each source into Eq. 20. The best constraints involves utilizing source J1630-4233 with optical data of r.v. is $m_g \leq 3 \times 10^{-23} eV/c^2$.

Next, we delve into the examination of the coefficient \bar{s}_{jm} . If only the simplest case is considered, which means only \bar{s}_{00} is a non-zero coefficient, it holds:

$$\bar{s}_{00} = \frac{-\frac{\Delta c}{c}}{\frac{1}{2}Y_{00}}. \quad (21)$$

Substituting the results of the joint analysis yields \bar{s}_{00} to $-3.4 \times 10^{-11} \leq \bar{s}_{00} \leq 1.5 \times 10^{-11}$ ($-3.5 \times 10^{-11} \leq \bar{s}_{00} \leq 1.6 \times 10^{-11}$), which is better than the result calculated in Liu et al. (2020). For the general case, employing 14 values for substitution into equation 4 provides limitations for all \bar{s}_{jm} coefficients. However, this particular calculation will be conducted in a distinct study.

8 DISCUSSION

The methodology outlined in this paper showcases the potential to confine $\Delta c/c$ within the realm of 10^{-12} , surpassing outcomes attained through GW dispersion. However, it falls short by approximately three to four orders of magnitude compared to the constraint

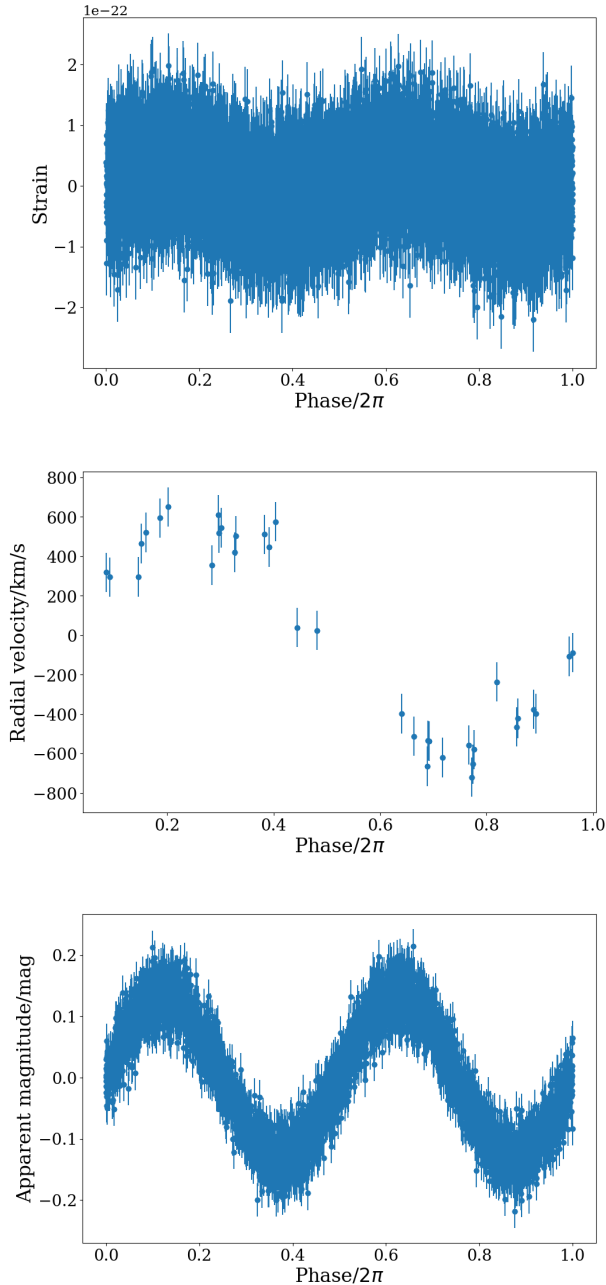


Figure 3. Phase-folded signals with error bar: Upper panel: GW data with 1.2×10^8 s sampling frequency of 10^{-1} Hz; middle panel: 35 r.v. data uniformly scattered randomly within the GW observation duration; lower panel: 5000 a.m. data for the same distribution as r.v.. For clearer visualization, the GW panel has been down-sampled to 0.1% of its original resolution. The r.v. measurement requires high quality spectrum and thus the data points are much fewer compared to that of a.m..

utilizing the time lag between GW and GRB. In the subsequent discussion, we discuss different aspects that would strengthen this method.

As depicted in Table 4, the data sizes for r.v. typically tend to fall within the range of approximately 10 to 100, whereas the data sizes for a.m. typically scale up to hundreds or even surpass a thousand. Employing source J0533+0209 once more, we experimented

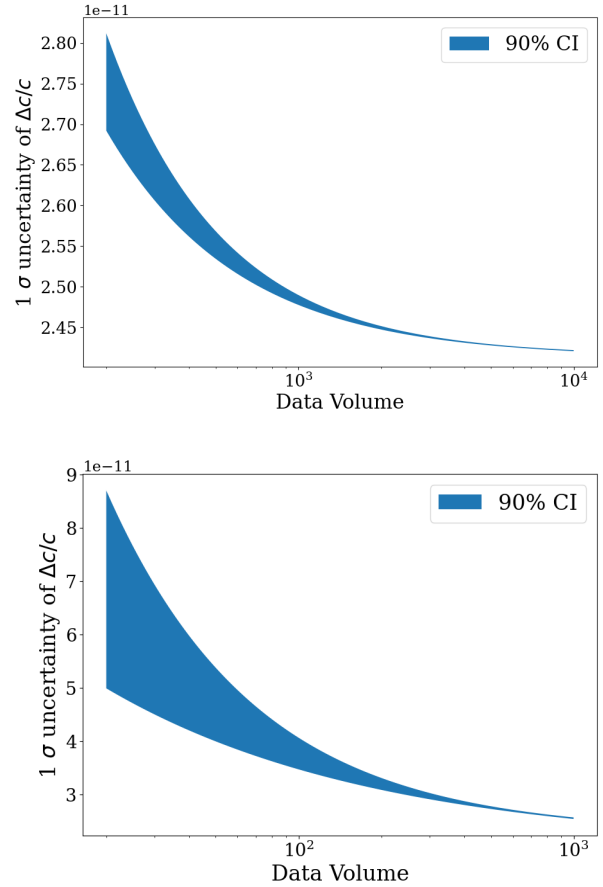


Figure 4. Diagram of the uncertainty of $\Delta c/c$ after the change of optical data volume.

by adjusting the data size for a.m. within the range of 100 to 10,000, while varying the data size for r.v. from 10 to 1,000. Employing the identical methodology as in the preceding section, each dataset was simulated 50 times to derive the distribution reflecting the ultimate standard deviation of the outcomes, as depicted in Figure 4. Similarly, we varied the uncertainties of r.v. and a.m. within two magnitudes and simulated each data set 50 times to obtain the distribution of the standard deviation of $\Delta c/c$ as shown in Figure 5. As the volume of data grows and quality enhancements are implemented, discernible improvements are evident in the simulation results, characterized by a decreased standard deviation and enhanced stability. Based on the above discussion, it is apparent that enhancing the quality of optical data may not significantly optimize the final results.

Increasing the number of sources presents another viable method. With reference to the relationship described in equation 19, we can roughly estimate the association between the number of sources, denoted by N_s , and the standard deviation of $\Delta c/c$ as:

$$\sigma_{\Delta c/c} \propto 1/\sqrt{N_s}. \quad (22)$$

As LISA runs, more VBs will be discovered. In addition, the eclipsing binaries are not considered in this paper in order to simplify the model. In fact, if the theoretical function of the a.m. variation of the eclipsing binaries is known which can be accomplished using the Phoebe package (Prša & Zwitter 2005), it can also be fitted to

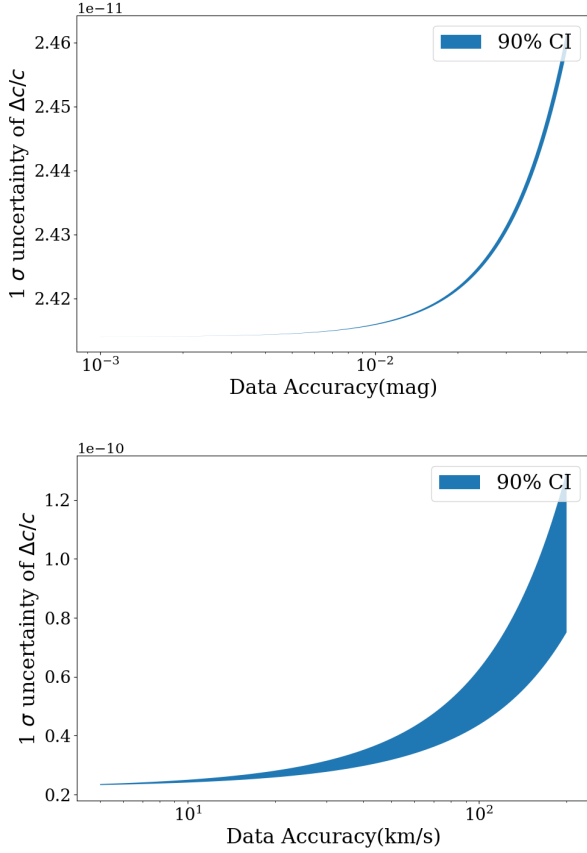


Figure 5. Diagram of the uncertainty of $\Delta c/c$ after the change of optical data uncertainty.

constrain the phase difference. Based on our assessment, it seems plausible to include data gathered from at least 8 sources in the dataset.

Overall, our method is astrophysical model independent which constrains c_{GW} with better accuracy. In addition, the use of more sources allows a more precise constraint on the parameter of local Lorentz violation. When analyzing the graviton mass, utilizing gravitational waves with lower frequencies leads to improved constraints on the mass.

However, the final accuracy of this method is limited by the distance of the source. Compared to GRBs, whose distances are on the order of 10 Mpc, and VBs, whose distances are generally on the order of kpc, lead to final results that are 3-4 orders of magnitude larger than GRB. Also, a drawback of this one method is that the distance of the VBs cannot reach the Mpc magnitude, so the results obtained by optimizing the data are expected to be improved by only 1-2 orders of magnitude and cannot reach the accuracy obtained by GRB.

It is worth noting that $\phi_s = 10^{-3}$ rad is the best case, while the average value of ϕ_s uncertainties is 0.1 rad. However, these uncertainties are estimated solely with GW data, while the sky position can be determined much better with optical observations, which is highly correlated with ϕ_s in GW inference. Therefore, the value reported from Huang et al. (2020) should be considered as a conservative upper limit on $\delta\phi_s$.

The method we proposed here can be easily transplanted into super

black hole binaries (SBHB), where the distance can be in the order of 100Mpc, and thus results in constraint in $\Delta c/c$ orders of several orders of magnitude better. SBHB are believed to exist in the center of merged Galaxies, with masses from 10^6 to 10^{10} solar masses. When the binary separation is close to pc scale, and the orbital period is \sim years, such systems are expected to emit GW in the nano-Hz band, which enters the range of Pulsar Timing Arrays (PTA) (Jaffe & Backer 2003). On the other hand, SBHB also may exhibit themselves in EMW bands, as dual AGNs, or AGNs which show periodic light curves. There are two such examples: Mrk 915 and MCG+11-11-032 (Severgnini et al. 2022). They are believed to possess SBHB with masses $M \sim 10^8 M_\odot$ and $M \sim 5 \times 10^8 M_\odot$, red-shift $z = 0.024$ and $z = 0.0362$, distance $d = 102.8$ Mpc and $d = 155.0$ Mpc (Take the Hubble constant as $H_0 = 70 \text{ km} \cdot \text{s}^{-1} \cdot \text{Mpc}^{-1}$), orbital period $T = 35$ months and $T = 25$ months. The expected GW strain from them is 1.5×10^{-16} and 1.9×10^{-15} . Which could be detectable with PTA in the near future (Enoki et al. 2004)⁶.

ACKNOWLEDGEMENTS

We would like to thank Prof. Yi-Ming Hu for his helpful comments and manuscript revision. This work is supported by the Chinese Academy of Sciences (Grant No. E329A3M1 and E3545KU2).

DATA AVAILABILITY

The data underlying this article will be shared on reasonable request to the corresponding author.

REFERENCES

- Abbott B. P., et al., 2017a, Physical review letters, 119, 161101
 Abbott B. P., et al., 2017b, The Astrophysical Journal Letters, 848, L13
 Abbott B. P., et al., 2019, Physical review letters, 123, 011102
 Abbott R., et al., 2023, Physical Review X, 13, 041039
 Amaro-Seoane P., et al., 2023, Living Reviews in Relativity, 26, 2
 Barke S., Wang Y., Delgado J. J. E., Tröbs M., Heinzl G., Danzmann K., 2014, arXiv preprint arXiv:1411.1260
 Brown W. R., Kilic M., Prieto C. A., Kenyon S. J., 2010, The Astrophysical Journal, 723, 1072
 Brown W. R., Kilic M., Hermes J., Prieto C. A., Kenyon S. J., Winget D., 2011, The Astrophysical Journal Letters, 737, L23
 Brown W. R., et al., 2020, The Astrophysical Journal, 889, 49
 Burdge K. B., et al., 2019a, Nature, 571, 528
 Burdge K. B., et al., 2019b, The Astrophysical Journal Letters, 886, L12
 Burkart J., Quataert E., Arras P., Weinberg N. N., 2013, Monthly Notices of the Royal Astronomical Society, 433, 332
 Carrettoni M., Cremonesi O., 2010, Computer Physics Communications, 181, 182
 Ciolfi R., Siegel D. M., 2015, arXiv preprint arXiv:1505.01420
 Cornish N., Blas D., Nardini G., 2017, Physical review letters, 119, 161102
 Cutler C., 1998, Physical Review D, 57, 7089
 Cutler C., et al., 1993, Physical Review Letters, 70, 2984
 Cutler C., Hiscock W. A., Larson S. L., 2003, Physical Review D, 67, 024015
 Einstein A., 1916, Sitzungsber. Preuss. Akad. Wiss. Berlin (Math. Phys.), 184, 1916
 Einstein A., 1918, Sitzungsber. Preuss. Akad. Wiss. Berlin, 154, 1918
 Enoki M., Inoue K. T., Nagashima M., Sugiyama N., 2004, The Astrophysical Journal, 615, 19

⁶ We calculate the SNR with the software package GW-Universe Toolbox (Yi et al. 2022).

- Fan X.-L., Liao K., Biesiada M., Piórkowska-Kurpas A., Zhu Z.-H., 2017, *Physical Review Letters*, 118, 091102
- Fuller J., Lai D., 2012, *Monthly Notices of the Royal Astronomical Society*, 421, 426
- Geier S., et al., 2013, *Astronomy & Astrophysics*, 554, A54
- Goyal S., Haris K., Mehta A. K., Ajith P., 2021, *Physical Review D*, 103, 024038
- Hendriks K., Yi S.-X., Nelemans G., 2023, *Astronomy & Astrophysics*, 672, A74
- Hermes J., et al., 2012, *The Astrophysical Journal Letters*, 757, L21
- Huang S.-J., et al., 2020, *Physical Review D*, 102, 063021
- Jaffe A. H., Backer D. C., 2003, *The Astrophysical Journal*, 583, 616
- Kilic M., Brown W. R., Hermes J., Allende Prieto C., Kenyon S., Winget D., Winget K., 2011, *Monthly Notices of the Royal Astronomical Society: Letters*, 418, L157
- Kilic M., Brown W. R., Gianninas A., Hermes J., Allende Prieto C., Kenyon S., 2014, *Monthly Notices of the Royal Astronomical Society: Letters*, 444, L1
- Kostelecký V. A., Mewes M., 2016, *Physics Letters B*, 757, 510
- Kupfer T., et al., 2018, *Monthly Notices of the Royal Astronomical Society*, 480, 302
- Larson S. L., Hiscock W. A., 2000, *Physical Review D*, 61, 104008
- Li X., Hu Y.-M., Fan Y.-Z., Wei D.-M., 2016, *The Astrophysical Journal*, 827, 75
- Liu X., He V. F., Mikulski T. M., Palenova D., Williams C. E., Creighton J., Tasson J. D., 2020, *Physical Review D*, 102, 024028
- Loève M., 2017, *Probability theory*. Courier Dover Publications
- Maggiore M., 2007, *Gravitational waves: Volume 1: Theory and Experiments*. OUP Oxford
- Mewes M., 2019, *Physical Review D*, 99, 104062
- Napiwotzki R., 2009, in *Journal of Physics: Conference Series*. p. 012004
- Parseval M.-A., 1806, *Mém. prés. par divers savants, Acad. des Sciences, Paris*, (1), 1, 638
- Provcenal J. L., et al., 1997, *The Astrophysical Journal*, 480, 383
- Prša A., Zwitter T., 2005, *The Astrophysical Journal*, 628, 426
- Ren L., Li C., Ma B., Cheng S., Huang S.-J., Tang B., Hu Y.-m., 2023, *The Astrophysical Journal Supplement Series*, 264, 39
- Rezzolla L., Kumar P., 2015, *The Astrophysical Journal*, 802, 95
- Rieke F., Warland D., Van Steveninck R. d. R., Bialek W., 1999, *Spikes: exploring the neural code*. MIT press
- Robson T., Cornish N. J., Liu C., 2019, *Classical and Quantum Gravity*, 36, 105011
- Ruan W.-H., Guo Z.-K., Cai R.-G., Zhang Y.-Z., 2020, *International Journal of Modern Physics A*, 35, 2050075
- Scientific L., et al., 2016, *Physical review letters*, 116, 221101
- Scientific L., Collaboration V., Abbott B., et al., 2018, *Physical Review Letters*, 121, 129901
- Severgnini P., et al., 2022, *Memorie della Società Astronomica Italiana Journal of the Italian Astronomical Society*, p. 74
- Tsang D., Read J. S., Hinderer T., Piro A. L., Bondarescu R., 2012, *Physical Review Letters*, 108, 011102
- Vallenari A., et al., 2023, *Astronomy & Astrophysics*, 674, A1
- Wagg T., Breivik K., de Mink S. E., 2022, *The Astrophysical Journal Supplement Series*, 260, 52
- Will C. M., 1998, *Physical Review D*, 57, 2061
- Yi S.-X., Nelemans G., Brinkerink C., Kostrzewa-Rutkowska Z., Timmer S. T., Stoppa F., Rossi E. M., Zwart S. F. P., 2022, *Astronomy & Astrophysics*, 663, A155
- Yu H., Weinberg N. N., Fuller J., 2020, *Monthly Notices of the Royal Astronomical Society*, 496, 5482

APPENDIX A: SIMULATING THE NOISE

For an arbitrary noise, the power is defined as:

$$P = \lim_{T \rightarrow \infty} \frac{1}{T} \int_{-\infty}^{\infty} |n(t)|^2 dt. \quad (\text{A1})$$

Parseval's theorem tells us that we can re-write the average power as follows (Parseval 1806):

$$P = \lim_{T \rightarrow \infty} \frac{1}{T} \int_{-\infty}^{\infty} |n(f)|^2 df. \quad (\text{A2})$$

Then the power spectral density is simply defined as the integrand above (Rieke et al. 1999):

$$S(f) = \lim_{T \rightarrow \infty} \frac{1}{T} |n(f)|^2. \quad (\text{A3})$$

Which means:

$$n(f) = \sqrt{S(f)} \cdot T e^{i\theta_f}, \quad (\text{A4})$$

where θ_f is a random phase (Carrettoni & Cremonesi 2010). Then the noise can be obtained using the inverse Fourier transform as follows:

$$n(t) = \mathcal{F}^{-1}[n(f)]. \quad (\text{A5})$$

However, if only consider noise within a small frequency Δf , we have:

$$\begin{aligned} P &= \int_{-\infty}^{\infty} S(f) df \\ &= S(f) \Delta f \end{aligned} \quad (\text{A6})$$

Assume that the noise is normally distributed, we have:

$$\begin{aligned} P &= \lim_{T \rightarrow \infty} \frac{1}{T} \int_{-\infty}^{\infty} |n(t)|^2 dt \\ &= \lim_{T \rightarrow \infty} \frac{1}{T} \int_{-\infty}^{\infty} E(|n(t)|^2) dt \\ &= \sigma_n^2 \lim_{T \rightarrow \infty} \frac{1}{T} \int_{-\infty}^{\infty} dt \\ &= \sigma_n^2 \end{aligned} \quad (\text{A7})$$

Combining Eq. A6 and Eq. A7, we have:

$$\sigma_n = \sqrt{S(f) \Delta f}. \quad (\text{A8})$$

The standard deviations of the noise simulated by the two methods are 5.3×10^{-23} and 3.76×10^{-23} . Therefore we think the second method is simpler and accurate enough.

This paper has been typeset from a $\text{\TeX}/\text{\LaTeX}$ file prepared by the author.